JAAS

COMMUNICATION

View Article Online
View Journal | View Issue

Cite this: J. Anal. At. Spectrom., 2025, 40, 3023

Received 23rd July 2025
Accepted 15th September 2025

DOI: 10.1039/d5ja00284b

rsc.li/jaas

Ultrafast LIBS elemental imaging: a new tool for pedogenesis studies in highly polluted anthropogenic soils

Clément Noel,[a] Hermine Huot,[b] César Alvarez-Llamas,[a] Marc Offroy,[c] Françoise Watteau,[d] Ludovic Duponchel *[e] and Vincent Motto-Ros *[a]

In this communication, we report the first LIBS imaging of soil thin sections at 25 μm resolution over 25 cm^2 with a 100 Hz acquisition rate. Coupled with micromorphology, this approach enables high-throughput elemental mapping, enhancing the analysis of soil structure, composition, and anthropogenic influences through nearly 4 million laser shots.

In recent years, the success of NASA's Martian exploration missions has catalysed unprecedented advances in the application of laser-induced breakdown spectroscopy (LIBS).[1] Notably, LIBS imaging has emerged as a benchmark technique for elemental mapping,[2–4] while the development of high-performance portable instruments has further accelerated its deployment across diverse analytical contexts.[5–7] One prominent area of portable instruments application lies in soil analysis, where the value of conducting *in situ* measurements is widely recognized.[8–11] This has led to a growing body of research across diverse environmental settings. Notably, most of these studies underscore the considerable complexity of soil matrices and the inherent challenges in obtaining reliable analytical results, particularly when quantitative analysis is required. These difficulties are largely attributed to matrix effects, along with factors such as moisture content, soil heterogeneity, and issues of sample repre-sentativeness.[12–15]

In this article, we propose a novel approach to applying LIBS for soil analysis. We therefore propose employing LIBS imaging to characterize a soil thin section, offering a detailed visualization of the soil's structure and composition down to a depth of approximately ten centimeters. Micro-morphology, the study of undisturbed soils or sediments at a microscopic level using thin sections, is a useful tool in soil science and archaeology. It provides valuable information about soil formation and functioning processes (*e.g.* mineral weathering, organic matter degradation, aggregation and root/soil interactions), as well as the influence of human activities such as modification of soil organization, introduction of artefacts and/or pollution. Its relevance to the study of early pedogenesis of anthropogenic soils has been demonstrated.[16] In this context, combining microscopic observations of the microstructure with elemental analyses helps to identify the natural or anthropogenic constituents of soil and how they evolve. In polluted soils, elemental mapping can be used to locate potentially toxic elements and determine their bearing phases. This complements the chemical extractions carried on bulk soils, which are used to assess the risk of transfer. For this purpose, analytical techniques such as scanning electron microscopy coupled with energy dispersive X-ray spectroscopy (SEM-EDX) or electron probe microanalysis (EPMA) are traditionally used for quantitative spot analysis or elemental mapping of specific areas of thin sections. Attempts have been made to use laser ablation ICP-MS on thin sections to measure trace elements on specific micro-morphological features with a low detection limit,[17] and EXAFS has been used to determine their speciation.[18] Micro-XRF has been demonstrated to provide elemental maps at the scale of thin sections or specific areas in order to study the distribution of metals in soil aggregates,[19] at the root/soil interface,[20] and in archaeological metal remains.[21] While these approaches offer high analytical precision, they are less suited for large-area investigations and are often limited by the considerable time required to process extensive vertical profile.

In this study, we present, to the best of our knowledge, the first application of high-speed LIBS imaging to a soil thin section. The results are striking: approximately 7 cm of soil profile were mapped at a micrometer-scale resolution (25 μm), covering a surface area of more than 20 cm^2. Notably, the analysis was conducted on a thin section approximately 30 μm

[a]Université Claude Bernard Lyon 1, Institut Lumière Matière, UMR 5306, CNRS, Villeurbanne 69622, France. E-mail: vincent.motto-ros@univ-lyon1.fr
[b]IRD, CNRS, Sorbonne Université, Université Paris Est Creteil, INRAE, Institute of Ecology and Environmental Sciences of Paris (iEES-Paris), F-75005 Paris, France
[c]Université de Lorraine, CNRS, LIEC, F-54000 Nancy, France
[d]Université de Lorraine, INRAE, LSE, F-54000 Nancy, France
[e]Univ. Lille, CNRS, UMR 8516 – LASIRE – Laboratoire de Spectroscopie pour Les Interactions, La Réactivité et L'Environnement, Lille, F-59000, France. E-mail: Ludovic.duponchel@univ-lille.fr

thick, enabling precise spatial alignment between optical and elemental images. We show that micro-LIBS imaging offers unprecedented insight into the distribution and colocalization of multiple metals with exceptional spatial accuracy, particularly at interfaces between distinct soil layers, within cracks, and along soil–root boundaries. This approach opens a promising new avenue for advanced soil analysis and environmental research.

Material and methods

Sample

The analysed sample was collected from a soil profile developing on the site of a former iron industry settling pond in Lorraine, France. Abandoned since the 1950s, the site has since been colonized by a deciduous forest, despite the presence of high concentrations of potentially toxic metal elements in the industrial substrate. To investigate soil formation processes, along with the speciation, mobility, and bioavailability of these metals, a multi-scale approach combining field observations and comprehensive physico–chemical characterizations was employed.[22,23] The soil organization was first characterized in the field along a vertical profile extending from the surface to approximately 2 meters in depth. As illustrated in Fig. 1a, the profile comprises a sequence of layers exhibiting distinct structures and colors, reflecting the successive deposition of sludges of varying origins, capped by an organo-mineral layer enriched in organic matter derived from surface vegetation. Twelve contrasting layers were sampled throughout the profile and analysed for their elemental composition, organic geochemistry, and mineralogical content, providing key insights into soil formation processes. To investigate the soil microstructure, undisturbed vertical samples were collected at various depths using Kubiena boxes (9 × 6 cm). From each sample, a thin section (30 μm thick, 9 × 6 cm) was prepared following the protocol established by Murphy,[24] which involved sequential drying through acetone substitution, dehydration, and vacuum impregnation with polyester resin. The consolidated blocks were then bisected, and one half was mounted on a glass slide of identical dimensions and ground down to obtain a 30 μm thick section. Microscopic examination of the thin sections using a stereomicroscope (Leica MFLZIII) enabled the identification of soil structural features (*e.g.*, laminar, particulate, or aggregated arrangements), as well as micromorphological characteristics including microstructures, voids, organic residues, roots, mineral inclusions, and technogenic materials. Selected regions of interest within the thin sections were further analysed for their elemental com-position using scanning electron microscopy coupled with energy-dispersive X-ray spectroscopy (SEM-EDS).[25] The thin section analyzed in this study was sampled from a depth of 60 to 70 cm and reveals a grey laminated layer several centimeters thick between two darker layers (Fig. 1c), hereafter designated as L3′, L4, and L5 (see zoom in Fig. 1b). For each of these layers, bulk analyses were conducted using dry combustion for organic elements, ICP-OES for major and minor elements, and ICP-MS for trace ele-ments.[22] Elemental concentrations for layers L3′, L4, and L5 are provided in SI (Table S1). The results highlight a distinct elemental composition in relation with variations in the iron-making process. The profile consists of a succession of layers with contrasting compositions: the friable dark-coloured layers (L3′ and L5) are enriched in manganese, while the compact laminated light-coloured layer (L4) is dominated by iron, calcium, and silicon, with elevated concentrations of lead, zinc, and tin. Layer 4 is also marked by the presence of anthropogenic organic matter, including waste oils, greases, and lubricants from industrial processes, as well as the likely presence of ferrocyanide.[23,26]

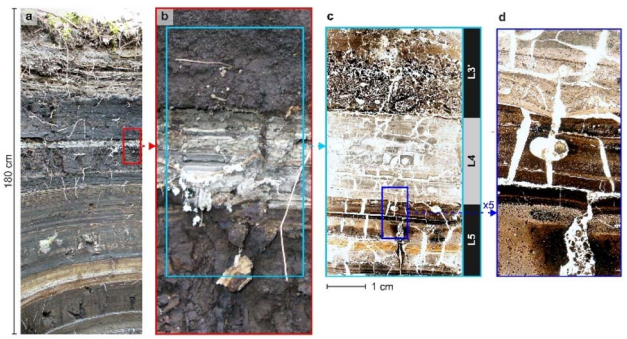

Fig. 1 Soil sample profile developed on steelmaking sludge (Lorraine, France). (a) Global profile view covering a height of almost 2 m. (b) Zoom on the region of interest showing a grey layer with a laminar structure (L4) surrounded by black layers (L3′ and L5). (c) Thin section, analysed by LIBS, showing the particulate structure of layer 3 and the laminar structure of layers 4 and 5. (d) ×5 zoom of the region indicated in (c) showing the presence of cracks and roots.

LIBS imaging experiment

The general protocol and the LIBS instrument used for this study have already been described in several publications.[27–29] Briefly, we used a Nd:YAG laser (Centurion GRM, Lumibird) with 7 ns pulse duration and 100 Hz repetition rate, emitting at the fundamental wavelength (1064 nm). A ×15 magnification objective microscope (LMM-15X-P01, Thorlabs) was used to focus the laser beam onto the sample surface, and the sample was moved using a motorized XYZ stage during the scanning sequence. An energy of 700 μJ was set for all the acquisitions, with an argon flow of 0.8 L min^{-1} to avoid surface contamination by ablated material redeposition of the previous laser shots and to improve the sensitivity by better plasma confinement. The experiment was performed at room temperature and ambient pressure. For the shown LIBS imaging results, the step size between each laser shot was fixed to 25 μm. The entire LIBS imaging setup was controlled by a homemade software developed in the LabVIEW environment, which allowed the monitoring of the experimental parameters (laser energy, position of the sample, stability of the plasma, *etc.*) and the setting of automated scan sequences. The plasma emission was collected by two lens-fiber systems, both coupled to a spectrometer. Two Czerny–Turner spectrometers coupled to ICCD cameras (Istar, Andor Technology) were used. The first spectrometer (A),

a Shamrock 303i (Andor Technology), with a 1200 L mm^{-1} grating covered the 190–235 nm wavelength range; the second one (B), a Shamrock 500i (Andor Technology), was configured with a 600 L mm^{-1} grating covering the 278–358 nm spectral range. With such configurations, a spectral resolution of about 0.15 nm could be achieved for both spectrometers. In addition, both ICCD cameras were synchronized to the Q-switch of the laser. For spectrometer A, a gain of 1500 was applied, with a delay and a gate width of 0.8 μs and 5 μs, respectively. For spectrometer B, a gain of 1000 was set, with a delay and a gate width of 1 μs and 5 μs, respectively. The spectral ranges of the two spectrometers were chosen to facilitate in priority the detection the zinc (Zn), and cadmium (Cd) from the spectrometer A, as well as lead (Pb), tin (Sn) and manganese (Mn) from spectrometer B. All detection parameters are listed in the SI (Table S2).

LIBS signal and extraction

Typical single-shot spectra obtained from the three layers L3′, L4 and L5 are shown in Fig. 2. As can be seen on the spectra, carbon (C), silicon (Si), calcium (Ca), magnesium (Mg), aluminum (Al), manganese (Mn), zinc (Zn), and lead (Pb) are well detected, as well as other elements such as iron (Fe), cadmium (Ca), and tin (Sn). It is important to note that these spectra are single-shot spectra, so they do not reflect the average (or overall) composition of each layer. Barium (Ba), copper (Cu), cobalt (Co), titanium (Ti), and silver (Ag) were also detected but they are not visible in Fig. 2. Line selection was performed to avoid interference issues. The selected lines are tabulated in SI (Table S3). LasMap, a dedicated software developed in the Light and Matter Institute (Lyon, France) allows to handle the large amount of data collected and to extract elemental images from the raw spectra datasets.[30,31] This software includes different atomic and molecular databases that enable the fast identification of the emission lines observed in the raw spectra. After the line identification step, the net intensity of the lines is extracted to generate a 2D matrix (relative abundance image). This procedure is relatively fast, processing about 120.000 spectra per second. Finally, ImageJ software (National Institutes of Health, USA) was used to apply a false color scale to present a visual result in the form of elemental images.

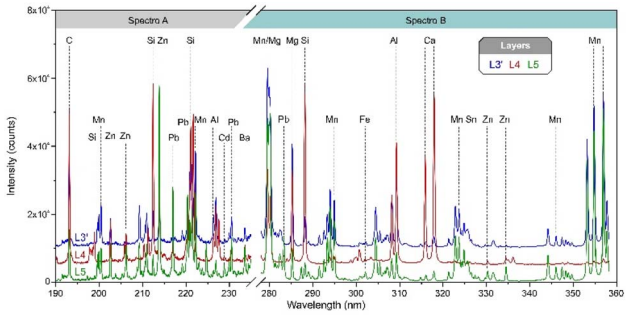

Fig. 2 Example of single shot spectra obtained in the three layers L3′ (blue), L4 (red) and L5 (green). The spectra have been shifted vertically for better clarity.

Results

LIBS elemental images obtained on the soil section for Pb, Sn, Fe, Zn, Cd, Mn, Cu, and Al are shown in Fig. 3, while images for Ca, Mg, Si, C, Ag, Ti, Ca, and Ba are presented in SI (Fig. S1). Compared to the bulk soil concentrations reported in Table S1 in SI, chromium (Cr) and arsenic (As) were not detected, likely due to strong spectral interferences, particularly with Mn.

Other elements such as strontium (Sr), nitrogen (N), and sulfur (S) were also not detected, as the spectral acquisition ranges used were not suitable for their detection. Finally, nickel (Ni) and antimony (Sb) were detected at a few isolated pixels, but the signal was too sparse to justify image reconstruction; thus, these are not shown here. The elemental images displayed in Fig. 3 correspond to a LIBS analysis sequence consisting of 1.200 × 3.000 shots, with a step size of 25 μm between each shot, resulting in a total of 3.6 million pixels acquired over two spectral ranges. This corresponds to approximately 10 hours of analysis time. These LIBS elemental images revealed the spatial heterogeneity of the distribution of major and trace elements, both between and within the layers (L3′, L4 and L5).

The distribution of the major elements confirmed that the dark layers (L3′ and L5) were enriched in Mn whereas the grey layer (L4) was enriched in Al, Si and Ca (Fig. 3 and S1 in SI), as shown by the bulk elemental analyses (Table S1 in SI). The distribution of C on the thin section showed a relative enrichment in the layer L4. However, it can be noted that the intensity of C as well as Si, Mg and probably Ca was high in the interstices between soil aggregates or soil laminae, probably revealing the influence of signals from the resin used to embed the soil, the glue or the glass slide. The distribution of Fe was more localized in some laminae within layers L4 and L5. Regarding the trace metallic elements, which can be present in high concentrations in this soil, the elemental images highlighted the vertical stratification of their distribution as well as some spots of metal concentration. The LIBS analyses confirmed that layer L4 was enriched in some metals as Sn and Cd, as shown by the bulk analyses, but revealed that the distribution of Cd was concentrated in specific laminae at the top of the layer. Merged elemental images (Fig. 3c) displayed the varying composition of the laminae with areas enriched in one dominant metal and areas of colocalized metals.

Based on the elemental images shown in Fig. 3, it is straightforward to reconstruct vertical distribution profiles for each element. This can be achieved by summing the signal intensities across the width of the sample and normalizing the resulting values by the maximum intensity along the vertical axis (Fig. 4). These profiles reveal geochemical differentiation between the layers L3′, L4, and L5. In the upper layer (L3′), Mn appears to be dominant, with lower amounts of Al and Cu.

Layer L4 shows relatively elevated amounts of Pb, Sn, Fe, Zn, Cu, and Al, while L5 exhibits higher intensities of Pb, Mn, Fe, Zn, and Cu. The abrupt transitions observed between layers (particularly at the interfaces between L3′–L4 and L4–L5) underscore the stratified deposits of blast furnace sludge of varying composition and suggest limited vertical mixing

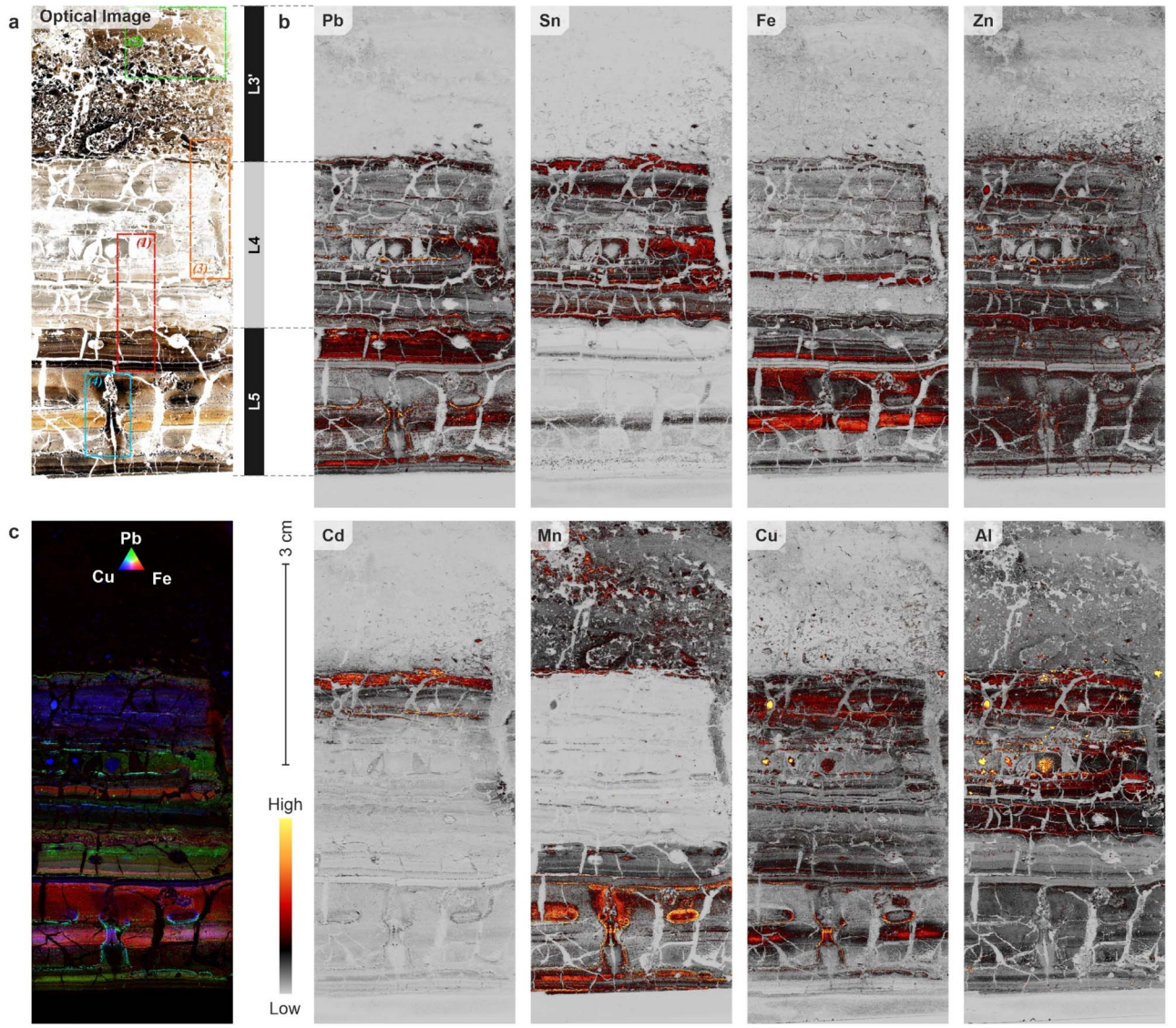

Fig. 3 LIBS elemental images of the studied soil thin section (a) optical image of the thin soil section. (b) Elemental images for some elements of interest. (c) Merged elemental images for Fe (red), Pb (green) and Cu (blue) highlighting the stratification of the soil profile.

between layers during the soil formation on these materials. These variations highlight the value of LIBS imaging for capturing fine-scale elemental distributions and for characterizing compositional heterogeneity in complex environ-mental samples. In addition to the vertical stratigraphy observed at the scale of the entire thin section, closer examination of specific regions reveals localized features in metal distribution. These results are shown in Fig. 5a–d, corresponding respectively to the areas labeled (1), (2), (3) and (4) in Fig. 3a.

For each subpanel, both the optical image and the relevant elemental maps are displayed. Fig. 5a illustrates the laminar structure and the co-localization of Pb, Sn, and/or Zn at the interface between layers L4 and L5. It shows that Zn appears to have a diffuse distribution in the soil matrix while Pb is more localized in very thin laminae or dots (Fig. 5a). Fig. 5b provides a zoomed-in view of the Mn-enriched upper layer L3′, revealing Co enrichment along the edges of finer-grained material. This close-up also emphasizes the particular structure of L3′, with particle sizes ranging from approximately 100 μm to 1 mm. Fig. 5c focuses on a crack extending through layer L4, filled with fine material originating from the overlying L3′ layer. It shows the migration of Mn-enriched particles into an Al-rich matrix, suggesting post-depositional mobilization. Finally, Fig. 5d shows a crack crossing the laminated L5 layer with, where Mn and Pb-enriched coatings and dark diffusion features extending into the adjacent Fe-rich matrix. These structures likely result from solubilization, transport, or diffusion processes occurring along fracture pathways.

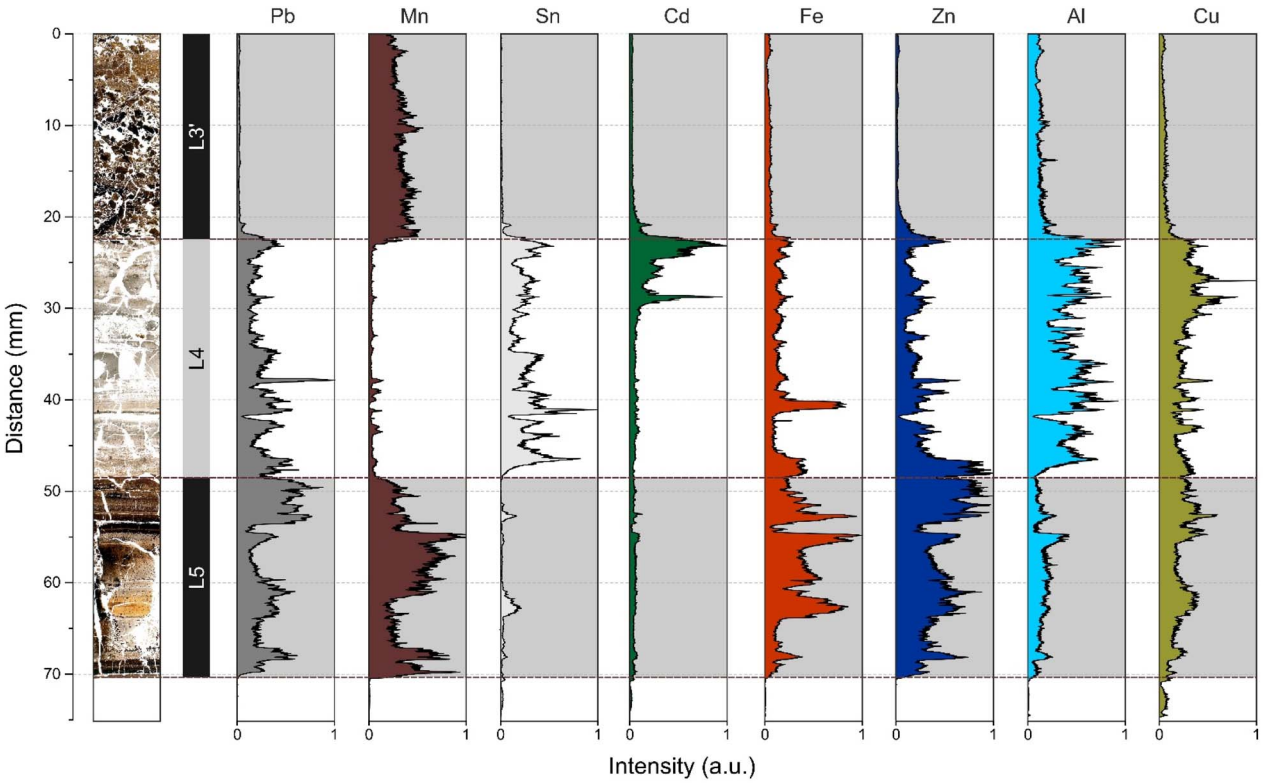

Fig. 4 Distribution of selected elements along the height of the sample. The profiles were obtained by summing the intensity across each row (*i.e.*, along the width of the sample) and normalizing the resulting values by the maximum intensity over the entire height.

Discussion

This study presents, for the first time to our knowledge, the application of LIBS imaging to the analysis of an undisturbed soil thin section. This methodological breakthrough is particularly noteworthy given the inherent challenges associated with laser ablation on fragile samples over large surface areas. One of the major advantages of this approach lies in its ability to preserve the original microstructure of the soil, enabling high-resolution elemental imaging without altering the sample integrity. The results are striking, offering an unprecedented combination of spatial resolution and elemental coverage over several square centimeters. Few, if any, analytical techniques currently available can deliver such detailed chemical information across such an extensive area at this scale. This capability allows for fine-grained interpretation of pedogenetic and environmental processes by coupling traditional micromorphological observations with elemental maps.

The method provides valuable insights into the vertical stratigraphy of anthropogenic soil layers and reveals microscale features such as coatings, cracks, and diffusion fronts indicative of material transformations and transport. Furthermore, it opens new avenues for investigating the localization and co-localization of potentially toxic metals within contaminated soils or sediments. Identifying metal-bearing phases at the microscale is critical for assessing environmental risk, especially in highly polluted contexts. Compared to conventional techniques such as SEM-EDS, μ-XRF, or EXAFS, LIBS imaging offers a unique balance between resolution, elemental sensitivity, and scanning speed, making it a promising tool for soil science and environmental diagnostics. Despite the clear strengths of the proposed approach, several technical aspects warrant consideration to optimize future implementations. The detection and interpretation of organic elements, particularly carbon, remain complex due to the constraints of sample preparation. As illustrated in SI Fig. S1, an enrichment in carbon is observed in layer L4; however, signals from the resin, adhesive, or glass substrate may contribute in certain areas, introducing potential artifacts. Similar uncertainties are noted for elements like silicon, calcium and magnesium, possibly originating from the glass slide, although aluminum appears unaffected. Additionally, each LIBS imaging session consumes the entire thin section. The use of lasers with shorter pulse durations could minimize ablation damage and improve spatial resolution, potentially down to 10 μm. Nevertheless, achieving this while maintaining acceptable acquisition times requires higher repetition rates, such as those under development using kHz systems with nanosecond pulses. The vast volume of data generated also calls for robust chemometric strategies to manage, analyze, and visualize the results effectively. Importantly, these challenges, while real, should not overshadow the exceptional quality and significance of the results presented here. The ability to produce high-definition, multi-elemental maps on undisturbed soil thin sections represents a major

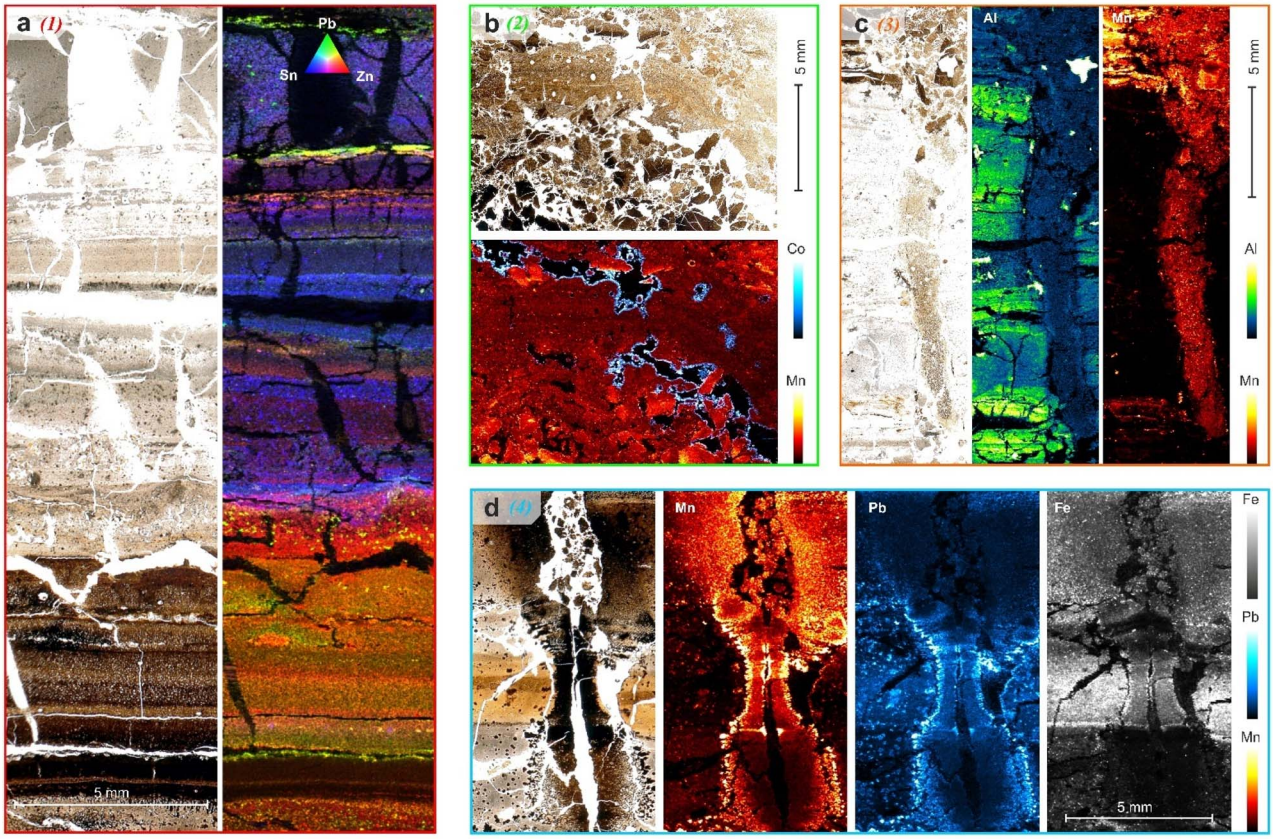

Fig. 5 Optical images and elemental LIBS images of some details of the thin section showing the distribution of metals: (a) in the laminar structure at the interface of layers 4 and 5, (b) in the layer 3′ with crumbly structure (c) in a crack in the layer 4 filled with fine material from layer 3′ and (d) in black coatings and diffusion figures at the edge of a crack crossing the laminar structure of the layer 5. Note that, (a), (b), (c) and (d) correspond to the regions labelled (1), (2), (3) and (4), respectively, in Fig. 3.

advance in the characterization of complex, heterogeneous soils. This methodological innovation opens new perspectives in environmental diagnostics and soil science, particularly for investigating anthropogenic or contaminated profiles. The demonstrated potential of LIBS imaging in this context far outweighs the current technical constraints, which are al-ready being actively addressed through ongoing instrumental and analytical developments.

Conclusion

This work demonstrates the first successful application of LIBS-based imaging on undisturbed soil thin sections, enabling high-resolution, multi-elemental mapping across large surface areas. The technique preserves the original micro-structure of the soil and provides detailed spatial information on the distribution of major and trace elements. It allows precise identification of metal colocalization at microscale interfaces such as cracks, laminae boundaries, and root–soil contacts. These results highlight the method's strong potential for supporting pedogenetic interpretations, evaluating pollutant distribution, and exploring geochemical processes in anthropogenic soils. Some limitations remain, including the interpretation of signals from organic elements due to sample preparation and the fact that laser ablation consumes the sample. However, the level of detail, richness of analytical information, and spatial precision achieved in this study marks a significant advancement. LIBS imaging stands out as a valuable addition to environmental and soil science workflows where both fine-scale resolution and extensive elemental coverage are required. Its integration into broader analytical strategies offers new perspectives for investigating soil formation and contamination dynamics in complex, human-influenced environments.

Author contributions

CN: data curation, formal analysis, software, writing – review & editing. HH: conceptualization, resources, validation, writing – original draft. CAL: data curation, formal analysis, writing – review & editing. MO: conceptualization, writing – review & editing. FW: resources, writing – review & editing. LD: conceptualization, validation, visualization, writing – original draft, writing – review & editing. VMR: conceptualization, funding acquisition, methodology, supervision, visualization, writing – original draft, writing – review & editing.

Conflicts of interest

There are no conflicts to declare.

Data availability

The data from this study are not freely available. We therefore ask you to contact the corresponding authors to discuss possible access options.

Supplementary information is available. See DOI: **https://doi.org/10.1039/d5ja00284b**.

Acknowledgements

This work was partially supported by the French region Rhônes Alpes Auvergne (Optolyse, CPER2016), the French "Agence Nationale de la Recherche" (ANR-22-CE27-0017 "MEMOar", ANR-20-CE17-0021 "dIAg-EM", ANR-20-CE05-0015 "Micro-Q-Li", ANR-23-CE42-0023 "AISLE"), and the French government "France 2030" initiative, under the DIADEM program managed by the "Agence Nationale de la Recherche" (ANR-22-PEXD-0014, "Libelul").

References

1 R. C. Wiens, S. Maurice, S. H. Robinson, A. E. Nelson, P. Cais, P. Bernardi, R. T. Newell, S. Clegg, S. K. Sharma, S. Storms, J. Deming, D. Beckman, A. M. Ollila, O. Gasnault, R. B. Anderson, Y. André, S. Michael Angel, G. Arana, E. Auden, P. Beck, J. Becker, K. Benzerara, S. Bernard, O. Beyssac, L. Borges, B. Bousquet, K. Boyd, M. Caffrey, J. Carlson, K. Castro, J. Celis, B. Chide, K. Clark, E. Cloutis, E. C. Cordoba, A. Cousin, M. Dale, L. Deflores, D. Delapp, M. Deleuze, M. Dirmyer, C. Donny, G. Dromart, M. George Duran, M. Egan, J. Ervin, C. Fabre, A. Fau, W. Fischer, O. Forni, T. Fouchet, R. Fresquez, J. Frydenvang, D. Gasway, I. Gontijo, J. Grotzinger, X. Jacob, S. Jacquinod, J. R. Johnson, R. A. Klisiewicz, J. Lake, N. Lanza, J. Laserna, J. Lasue, S. Le Mouélic, C. Legett, R. Leveille, E. Lewin, G. Lopez-Reyes, R. Lorenz, E. Lorigny, S. P. Love, B. Lucero, J. M. Madariaga, M. Madsen, S. Madsen, N. Mangold, J. A. Manrique, J. P. Martinez, J. Martinez-Frias, K. P. McCabe, T. H. McConnochie, J. M. McGlown, S. M. McLennan, N. Melikechi, P.-Y. Meslin, J. M. Michel, D. Mimoun, A. Misra, G. Montagnac, F. Montmessin, V. Mousset, N. Murdoch, H. Newsom, L. A. Ott, Z. R. Ousnamer, L. Pares, Y. Parot, R. Pawluczyk, C. Glen Peterson, P. Pilleri, P. Pinet, G. Pont, F. Poulet, C. Provost, B. Quertier, H. Quinn, W. Rapin, J.-M. Reess, A. H. Regan, A. L. Reyes-Newell, P. J. Romano, C. Royer, F. Rull, B. Sandoval, J. H. Sarrao, V. Sautter, M. J. Schoppers, S. Schröder, D. Seitz, T. Shepherd, P. Sobron, B. Dubois, V. Sridhar, M. J. Toplis, I. Torre-Fdez, I. A. Trettel, M. Underwood, A. Valdez, J. Valdez, D. Venhaus and P. Willis, *Space Sci. Rev.*, 2021, **217**, 4.
2 L. Jolivet, M. Leprince, S. Moncayo, L. Sorbier, C.-P. Lienemann and V. Motto-Ros, *Spectrochim. Acta, Part B*, 2019, **151**, 41–53.
3 V. Gardette, V. Motto-Ros, C. Alvarez-Llamas, L. Sancey, L. Duponchel and B. Busser, *Anal. Chem.*, 2023, **95**, 49–69.
4 B. Busser, S. Moncayo, J.-L. Coll, L. Sancey and V. Motto-Ros, *Coord. Chem. Rev.*, 2018, **358**, 70–79.
5 C. Fabre, *Spectrochim. Acta, Part B*, 2020, **166**, 105799.
6 J. Rakovský, P. Čermák, O. Musset and P. Veis, *Spectrochim. Acta, Part B*, 2014, **101**, 269–287.
7 R. S. Harmon, R. E. Russo and R. R. Hark, *Spectrochim. Acta, Part B*, 2013, **87**, 11–26.
8 R. T. Wainner, R. S. Harmon, A. W. Miziolek, K. L. McNesby and P. D. French, *Spectrochim. Acta, Part B*, 2001, **56**, 777–793.
9 X. T. Yan, K. M. Donaldson, C. M. Davidson, Y. Gao, H. Wu, A. M. Houston and A. Kisdi, *RSC Adv.*, 2018, **8**, 36886–36894.
10 A. Ismaël, B. Bousquet, K. Michel-Le Pierrès, G. Travaillé, L. Canioni and S. Roy, *Appl. Spectrosc.*, 2011, **65**, 467–473.
11 A. Wangeci, M. Knadel, O. De Pascale, M. H. Greve and G. S. Senesi, *J. Anal. At. Spectrom.*, 2024, **39**, 2903–2916.
12 G. S. Senesi and N. Senesi, *Anal. Chim. Acta*, 2016, **938**, 7–17.
13 P. R. Villas-Boas, M. A. Franco, L. Martin-Neto, H. T. Gollany and D. M. B. P. Milori, *Eur. J. Soil Sci.*, 2020, **71**, 805–818.
14 M. Ma, L. Fang, N. Zhao and X. Ma, *Chemosensors*, 2024, **12**, 40.
15 P. R. Villas-Boas, M. A. Franco, L. Martin-Neto, H. T. Gollany and D. M. B. P. Milori, *Eur. J. Soil Sci.*, 2020, **71**, 789–804.
16 F. Watteau, H. Huot, G. Séré, J. C. Begin, F. Rees, C. Schwartz and J. L. Morel, *Span. J. Soil Sci.*, 2018, **8**, 2606.
17 F. Scarciglia, D. Barca, R. De Rosa and I. Pulice, *Geoderma*, 2009, **152**, 113–126.
18 N. Janot, H. Huot, C. Rivard, M. Perrin, A. Noirault, Y.-T. Tang, F. Watteau and E. Montargès-Pelletier, *J. Hazard. Mater. Adv.*, 2025, **17**, 100609.
19 C. E. Gattullo, I. Allegretta, C. Porfido, I. Rascio, M. Spagnuolo and R. Terzano, *Environ. Sci. Pollut. Res.*, 2020, **27**, 22967–22979.
20 A. Voegelin, F.-A. Weber and R. Kretzschmar, *Geochim. Cosmochim. Acta*, 2007, **71**, 5804–5820.
21 B. Wouters, C. Makarona, K. Nys and P. Claeys, *Geoarchaeology*, 2017, **32**, 311–318.
22 H. Huot, M.-O. Simonnot, P. Marion, J. Yvon, P. De Donato and J.-L. Morel, *J. Soils Sediments*, 2013, **13**, 555–568.
23 H. Huot, P. Faure, C. Biache, C. Lorgeoux, M.-O. Simonnot and J. L. Morel, *Sci. Total Environ.*, 2014, **487**, 389–398.
24 S. Palle and D. Chappard, *J. Microsc.*, 1987, **147**, 213.
25 H. Huot, M. O. Simonnot, F. Watteau, P. Marion, J. Yvon, P. De Donato and J. L. Morel, *Eur. J. Soil Sci.*, 2014, **65**, 470–484.
26 H. Huot, M.-O. Simonnot and J. L. Morel, *Soil Sci.*, 2015, **180**, 182–192.
27 V. Motto-Ros, E. Negre, F. Pelascini, G. Panczer and J. Yu, *Spectrochim. Acta, Part B*, 2014, **92**, 60–69.
28 J. O. Cáceres, F. Pelascini, V. Motto-Ros, S. Moncayo, F. Trichard, G. Panczer, A. Marín-Roldán, J. A. Cruz, I. Coronado and J. Martín-Chivelet, *Sci. Rep.*, 2017, **7**, 1–11.

29 C. Fabre, D. Devismes, S. Moncayo, F. Pelascini, F. Trichard, A. Lecomte, B. Bousquet, J. Cauzid and V. Motto-Ros, *J. Anal. At. Spectrom.*, 2018, **33**, 1345–1353.
30 V. Motto-Ros, S. Moncayo, F. Trichard and F. Pelascini, *Spectrochim. Acta, Part B*, 2019, **155**, 127–133.
31 S. Moncayo, L. Duponchel, N. Mousavipak, G. Panczer, F. Trichard, B. Bousquet, F. Pelascini and V. Motto-Ros, *J. Anal. At. Spectrom.*, 2018, **33**, 210–220.